Multicompartmental Poroelastic Modelling for CSF Production and Circulation

John C. VARDAKIS[1], Brett TULLY[1], James BYRNE[2], Yiannis VENTIKOS[1, *]

* Corresponding author: yiannis.ventikos@eng.ox.ac.uk
1: Institute of Biomedical Engineering & Department of Engineering Science, University of Oxford, UK
2: Nuffield Department of Surgery, University of Oxford, UK

Abstract This study proposes the implementation of a Multiple-Network Poroelastic Theory (MPET) model for the purpose of investigating in detail the transport of water within the cerebral environment. The advantage of using the MPET representation is that it accounts for fluid transport between CSF, brain parenchyma and cerebral blood. They key novelty in the model discussed in the present study is the amalgamation of anatomically accurate *Choroid Plexus* regions, with their individual feeding arteries. This model is used to demonstrate the impact of aqueductal stenosis and atresia of the Foramina of Luschka and Magendie on the cerebral ventricles. The possible implications of treating such a condition with the aid of endoscopic third ventriculostomy are investigated and discussed.

Keywords: cerebrospinal fluid, choroid plexus, hydrocephalus, porous media, ventriculostomy, MRI

1. Introduction

1.1 Anatomy

The development of cerebral diseases such as Hydrocephalus, Alzheimer's and Parkinson's disease are unified by the theme of disruption of fluid transport within the brain (Tully B. B., 2010). The brain has two discrete fluid compartments, namely the interstitial fluid space (IFS) which immerses the neurons and glia and the cerebrospinal fluid (CSF) that fills the cerebral ventricles (Figure 1) and the external surfaces of the brain.

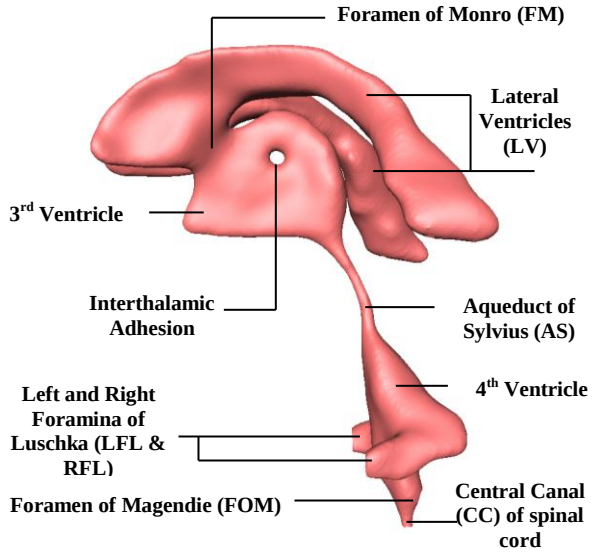

Figure 1 – Axial view of geometry of a human ventricular system (VS) showing key anatomical features. This is also the geometry of the VS used for the simulations presented herewith.

The Choroid Plexus (CP) is the main site of CSF production and is situated within the 3rd, 4th and the underside of the LV (See figure 2). CSF is also produced to a lesser degree by the bulk flow due to the pressure gradient within the brain parenchyma (Irani, 2009).

Once the CSF reaches the 4th ventricle, some of it exits through the central canal but the overwhelming proportion flows around the *tentorium cerebelli* in order for it to be absorbed by the arachnoid granulations and into the superior sagittal sinus (Rekate, 2008; Gupta S. S., 2010).

Since this work will incorporate a geometrically accurate CP in all the aforementioned locations, the arterial supplies to these plexuses have to be included. For the LV, the arterial supply is dominated by the anterior choroidal artery (ACA) and the medial and lateral posterior choroidal arteries (MpCA and LpCA). Likewise, the CP of the 3rd and 4th ventricle is supplied by the posterior cerebral and inferior cerebellar arteries (PCA and ICrA) respectively (Irani, 2009).

The normal circulation of CSF begins at the production sites of the CP of the LV, where it circulates in this region of the VS until it flows to the 3rd ventricle via the FM. It then passes through the Aqueduct of Sylvius (AS)

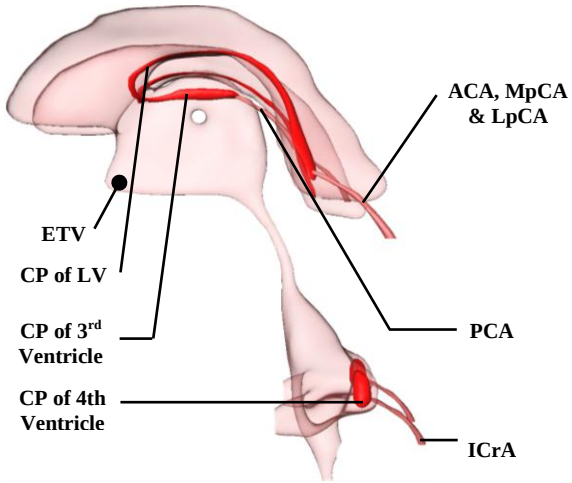

Figure 2 – View of the ventricular system along with the Choroid plexus of the lateral (LV), 3rd and 4th ventricles. The *arteries* supplying these plexuses are also shown. ETV is the location of perforation of the floor of the 3rd Ventricle during endoscopic third ventriculostomy.

to the 4th ventricle. Prior to exiting the RFL, LFL, FOM and CC, the CSF exiting the AS amalgamates with the CSF already being produced at the CP of the 4th ventricle (Irani, 2009; Howden, 2007). A depiction of the CP and selected arteries can be seen in Figure 2.

1.2 Acute Hydrocephalus

There is no formal definition of hydrocephalus (HCP). An accepted starting point would be to describe HCP as the active distension of the cerebral ventricular system due to the imbalance between production and circulation of CSF (Thompson, 2009; Rekate, 2008). It has no known cure and the most common treatment methods display high failure rates (Tully, 2010).

In this paper we examine the acute form of HCP. This is a type of obstructive HCP, with numerous possible locations of CSF flow obstruction such as: FM, FL, FOM and the AS. The latter is investigated in detail as it's the most commonly identifiable obstruction radiographically. Three degrees of obstructive severity are outlined, namely, open, mild and severe. The FOM and FL are also investigated, but in these cases only complete atresia is explored (Tully, 2010; Rekate, 2008; Gianetti, 2011).

1.3 Endoscopic Third Ventriculostomy (ETV)

ETV is used to drain CSF from the ventricles to the basal subarachnoid space when acute HCP is prevalent (Farin, 2006). Surgeons traditionally use shunting to treat HCP; however, this is liable to complications such as obstruction or infection (Thompson, 2009; Farin, 2006). There is strong evidence to suggest that ETV results in successful treatment as the percentage of shunt independence post-ETV varies between 50-91%. Another added advantage is that ETV can be performed to patients with previous histories of shunt failure with a high success rate (66%) (Farin, 2006). There are various forms of surgical techniques one can use for ETV, based on surgical trajectories and the comprehensive understanding of the anatomical-topographical aspects of the 3rd ventricle (Hellwig, 2005).

The operative procedure involves passing an endoscope into the LV via a burr hole with diameter in the range of $2-5$ *mm* in the frontal region. The endoscope's trajectory is aimed at the FM and finally to the floor of the third ventricle (Figure 2). During HCP, the net volume of the 3rd ventricle will have increased and its thin floor will have therefore been elongated. The floor is perforated in the midline once the clinoid recess is identified in order to avoid vascular injury. The opening is subsequently enlarged with a Fogarty catheter (Farin, 2006).

In this work, a computational model will be used to describe the dynamics of the cerebral environment driven by HCP. The effect of ETV is also investigated. The novelty associated with our computational method is that unlike current models aiming to describe HCP, the MPET framework adopted here can capture the effect of the cerebral blood network interacting with CSF and the surrounding tissue. Finally, anatomically accurate CP's are introduced along with their arterial supply to account better for the coupled CSF production – blood flow effect in those regions.

2. Methods

2.1 Anatomy acquisition

The three-dimensional anatomy of the VS, CP

and the arterial system was reconstructed from a series of (511(XY), 314(XZ), 511(YZ)) DICOM files produced from a T2-weighted MRI scan of a healthy male volunteer aged in his sixties. The images of the entire cranial area were acquired in the Sagittal, Axial and Coronal directions. The slice spacing was 0.5 mm. The acquired images were manually segmented for the VS using Amira (Mercury Computer Systems, San Diego, CA, USA) and the raw segmented geometry from this process was saved as an Stereo Lithography (STL) file (Figure 3). In order to preserve key anatomical features such as the AS, subsequent smoothing of the STL file was done using the open-source modelling software, Blender (The Blender Foundation, www.blender.org).

An advantage of using Blender is that duplicate vertices can be erased and in doing so reduce the size of the final STL file. Owing to its powerful individual nodal manipulation capabilities, Blender was also used to apply the local stenosis to the three-dimensional patient specific geometries for the cases involving the three degrees of HCP severity. It must be noted that the current standard voxel size produced from clinical imaging does not permit the accurate differentiation of different degrees of aqueductal stenosis.

Finally, inlets and outlet boundaries were created using **CFD-VisCART** (ESI Group, Paris, France), which was also used to generate non-conforming computational grids. The final smoothed STL file for an open AS (i.e. no stenosis) is seen in Figure 1.

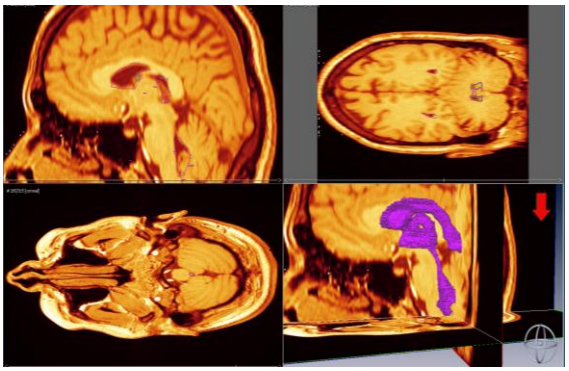

Figure 3 – The process of preparing the patient-specific ventricular system, choroid plexuses and respective arteries. The 4th quadrant depicts the output of the raw 3-D segmentation of the cerebral ventricles.

2.2 MPET computational model

Regulation of CSF and tissue displacement within the cerebral environment was modelled by considering a spatio-temporal model. MPET theory is actively used in geotechnical engineering to model materials which have naturally fractured fluid passages and which possesses both storage and transport porosities. These reservoirs intrinsically contain various subdivisions of permeabilities and are therefore aptly suited to a multiple-poroelastic network (Bai, 1993).

MPET amalgamates fundamental conservation of mass and momentum principles, stress-strain relationships, the Terzaghi effective stress principle and porous flow laws. In the system in question, a solid matrix (s) is permeated by $a = 1, \dots, A$ number of fluid networks. Each network has its own individual porosity (n^a), density (ρ^a), permeability (k^a) and finally fluid velocity relative to the aforementioned solid matrix $\left(\frac{w_i^a}{n^a}\right)$.

The complete system presents a highly non-linear set of equations which require vast computational effort. Fortunately, we are dealing with biological flows (CSF) and so acceleration frequencies can be neglected and this can simplify the system to a concise set of $A + 1$ equations (in vector notation):

$$\nabla \cdot \boldsymbol{\sigma}' - \sum_{a=1}^{A} \alpha^a \nabla p^a + \rho\left(b - \frac{\partial^2 u}{\partial t^2}\right) = 0 \qquad (1a)$$

$$\frac{1}{Q^a}\frac{\partial p^a}{\partial t} + \alpha^a \frac{\partial(\nabla \cdot u)}{\partial t} + \nabla \cdot \left[k^a \cdot \rho^a \left(b - \frac{\partial^2 u}{\partial t^2}\right) - k^a \cdot \nabla p^a\right] - \sum_{b=1, b\neq a}^{A} \dot{s}_{b\to a} = 0 \qquad (1b)$$

Here, $\boldsymbol{\sigma}'$ is the effective stress in the solid matrix; b is the local body force; u is the displacement of the solid matrix; $\rho = \sum_{a=1}^{A} n^a \rho^a + \rho_s(1-n)$ is the total density of the system; $n = \sum_{a=1}^{n} n^a$ is the total porosity of the combined fluid networks; ρ_s is the density of the solid; k is the isotropic permeability, Q is the combined compressibility of the system; $\frac{\partial(\nabla \cdot u)}{\partial t} = \dot{\epsilon}_{ij}$ is the strain in the solid matrix; α^a is the Biot parameter of the defined network a and finally $\dot{s}_{b\to a}$ is the rate of fluid exchange from network b to a (Tully B. V., 2010).

This transfer is governed by a hydrostatic pressure gradient.

The MPET framework strives to capture the independent nature of the fluid transfer within the brain. The quadruple MPET model takes into account the arterial blood network (a), the arteriole/capillary network (c), venous blood network (v) and extracellular/CSF network (e). To transform the system in equations $1a$ and $1b$ into the quadruple MPET system required, one sets $A = 4$ and $a = [a, c, v, e]$. In addition to this, further simplifications are made by assuming: a linear stress-strain relationship; isotropic permeability; no external forces on the system; negligible gravitational effects; stationary reference frame; quasi-steady system due to the large time scales in the development of HCP; physiology-derived constraints of specific directional transfer of water between networks in order to avoid breaches in continuity and finally a spherically symmetric (one dimensional) geometry. This gives the following simplified relationships for the new quadruple MPET system:

$$\frac{\partial^2 u}{\partial r^2} + \frac{2}{r}\frac{\partial u}{\partial r} - \frac{2}{r^2}u - \frac{1-2v}{2G(1-v)}\left(\alpha^a \frac{\partial p^a}{\partial r} + \alpha^c \frac{\partial p^c}{\partial r} + \alpha^v \frac{\partial p^v}{\partial r} + \alpha^e \frac{\partial p^e}{\partial r}\right) = 0 \quad (2a)$$

$$-k^a\left(\frac{\partial^2 p^a}{\partial r^2} + \frac{2}{r}\frac{\partial p^a}{\partial r}\right) + |\dot{s}_{a\to c}| = 0 \quad (2b)$$

$$-k^c\left(\frac{\partial^2 p^c}{\partial r^2} + \frac{2}{r}\frac{\partial p^c}{\partial r}\right) - |\dot{s}_{a\to c}| + |\dot{s}_{c\to e}| + |\dot{s}_{c\to v}| = 0 \quad (2c)$$

$$-k^v\left(\frac{\partial^2 p^v}{\partial r^2} + \frac{2}{r}\frac{\partial p^v}{\partial r}\right) - |\dot{s}_{c\to e}| + |\dot{s}_{e\to v}| = 0 \quad (2d)$$

$$-k^e\left(\frac{\partial^2 p^e}{\partial r^2} + \frac{2}{r}\frac{\partial p^e}{\partial r}\right) - |\dot{s}_{c\to v}| - |\dot{s}_{e\to v}| = 0 \quad (2e)$$

In the above, G is the shear modulus and v is the Poisson's ratio. In addition, if one observes this set of equations 2, there is an evident alternation of signs for the $|\dot{s}|$ terms. A negative/positive sign indicates an addition/loss of fluid to the network. This model allows for the natural incorporation of further, multiscalar, detail by involving cellular level interactions such as aquaporin-centred transport, believed to facilitate rapid absorption from CSF and ISF. However, the lack of reliable quantifiable data associated with such processes and the ambiguity surrounding the specifications of their presence do not currently warrant their immediate inclusion (Bulat, 2011).

2.3 Model Implementation

In this study, we account for the bulk ventricular motion of CSF (and arterial flow of blood) with the aid of finite-volume (FV) computational fluid dynamics (CFD), whereas we use the above mentioned MPET framework for processes taking place in the tissue. For the numerical discretisation of the latter, the model equations described by equations $2a$-$2d$ form a coupled, stiff linear system requiring implicit treatment. We employed a 2nd order central difference scheme; the spatial derivatives in the boundary conditions were of 1st order forward and backward difference schemes and finally the temporal elements were solved with a forward difference scheme. The base discretization involved 81 nodes along the (spherically symmetric) radial direction for this study – we have verified that this resolution is adequate.

This MPET solver is coupled with the multi-physics solver **CFD-ACE+** (ESI Group, Paris, France) in order to perform the CFD part of the simulations. The VS, CP and various artery domains are discretized into fine computational grids, suitable for CFD analysis. This was done with the aid of **CFD-VisCART** (part of the CFD-ACE+ suite). This is an unstructured adaptive Cartesian grid generation system suitable for very complex geometries (such as the patient specific VS, CP and artery systems in this study). For the entire system, over 2 million cells were used for each case of HCP and HCP with applied ETV. Grid independence analysis has shown that this resolution is adequate for the problem at hand.

Some constants that were used in this study are given in Table 1.

Parameter	Value	(units)
Density of CSF, ρ^e	997	kg/m^3
Dynamic viscosity of CSF, μ^e	8.9×10^{-4}	$N \cdot s/m^2$
Arterial Blood Pressure, p_{Abp}	100	$mmHg$

Table 1 – Table showing some of the fluid parameters used in the MPET numerical solver for CSF (at ~ 25°C) and arterial blood pressure.

3. Results

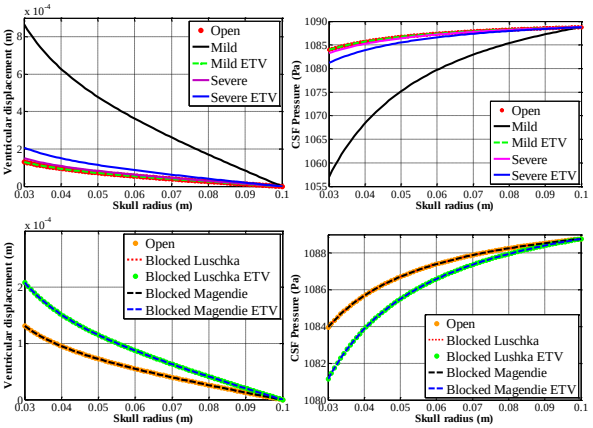

Figure 4 – The plots are comparing two sets of induced hydrocephalus. The plots in the 2nd and 3rd quadrants show the results for ventricular displacement and CSF pressure when varying the degree of aqueductal stenosis (open, mild and severe). The 1st and 4th quadrants show the same results for inducing complete occlusion in the RFL and FOM.

The results shown in Figure 4 show the first application of the MPET model to acute HCP and simultaneous application of ETV. The transfer of water between four networks to mimic the cerebral environment reveals interesting features. The 2nd and 3rd quadrants show the results of the ventricular displacement along with the corresponding CSF pressure for the three cases of stenosed aqueduct. The greatest displacement was witnessed for the mild case, which was $8.66 \times 10^{-4}\, m$. The mild case also exhibited the lowest ventricular CSF pressure, being $1057\, Pa$. The justification behind the mild case showing the largest ventricular displacement and lowest CSF pressure may be identified by further analysis of the Womersley and Reynolds numbers in §4. The CSF pressure converges to $1089\, Pa$ for all cases. The ventricular displacement decreases to 0 m at the skull, since this is imposed as a rigid, adult skull boundary condition (skull radius of 10 cm).

The 1st and 4th quadrant shows similar features as before. However, on this occasion, the results are shown for the cases of complete occlusion of the RFL and FOM. The aforementioned cases result in virtually identical ventricular displacement ($1.31 \times 10^{-4}\, m$) when left untreated (no ETV). The ventricular displacement and CSF pressure curve for the case of the occluded RFL is identical to that of the unobstructed case (Open) and occluded FOM. It seems that applying ETV in this case exacerbates the problem, as there is a proportional rise in ventricular displacement for both occluded cases to a maximum of $2.08 \times 10^{-4}\, m$. The pressure distributions of the ETV cases are on average less, as seen on the 4th quadrant of Figure 14. The convergence value is again $1089\, Pa$. What is evident from both sets of results is that the introduction of an occlusion to the RFL and FOM does not alter the ventricular displacement under the current simulations. The CSF pressure also remains unaltered in this case. For the aqueductal case, the results are more pronounced, and greater detail is required by introducing further parameters that can both quantitatively and qualitatively help provide better insight to the observations made.

The peak Reynolds number (Re_p) is obtained based on the peak velocity (v_p) and hydraulic diameter (D_h). D_h is given by $D_h = (4 \cdot Area)/Perimeter$. In this work, all cross sectional areas resembled an ellipse as $\frac{Axis_{major}(a)}{Axis_{minor}(b)} > 1\ \forall$ cross sections concerned. The perimeter of an ellipse was therefore used, and this is approximately given by $P_e = 2\pi\sqrt{(a^2 + b^2)/2}$.

Re_p is defined as:

$$Re_p = \frac{\rho^e \cdot v_p \cdot D_h}{\mu^e}\ ,$$

Where ρ^e and μ^e are the density and dynamic viscosity of CSF, as given in Table 1.

The largest Re_p number observed was 666.76 (Table 2) at the AS during the case of severe aqueductal stenosis. The LFL also had a high value, that of 197.52. This was during full occlusion of the RFL, mimicking a form of severe hydrocephalus of the 4th ventricle. Likewise, when the FOM was fully occluded, a Re_p value of 136.22 and 107.32 was witnessed for the LFL and RFL respectively. All Reynolds numbers were in the laminar range (Table 2 and 4). Consistently low values of peak Reynolds number were seen in the central canal, both with and without the application of ETV. Table 3 shows results for

the peak velocity of the central canal not exceeding $0.02\ m/s$.

A measure of the transient inertial to viscous forces was also utilized, namely the Womersley number, w_α. This is defined as:

$$w_\alpha = \sqrt{\frac{\rho^e \cdot \omega \cdot \left(\frac{D_h}{2}\right)^2}{\mu^e}} \ ,$$

where $\omega = 2\pi/T$ is defined as the pressure pulsation frequency ($T = 15s$ since we are considering the last iteration). When $w_\alpha < 1$, pressure is known to faithfully track the oscillating pressure gradient and the velocity profiles are almost parabolic. For $w_\alpha > 1$, the inertial forces are too large, and the velocity profiles do not succinctly follow the driving pressure gradient as they are phase-shifted in time relative to this gradient. As can be seen from Table 3, the w_α values for all the foramina of the 4th ventricle are greater than unity, indicating that the CSF flow is indeed of pulsatile nature, the fluctuations of which directly affect the final result of the simulation.

A pathogenic indicator of the degeneration state of the ventricular wall is sought in the Wall Shear stress (WSS). This is defined by:

$$\mathrm{WSS} = \mu^e \left(\frac{\partial u}{\partial y}\right)_{y=0} \ ,$$

Severity	$\mathbf{D_h}$ ($\times 10^{-3}$m)	$\mathbf{v_p}$ (m/s)	**WSS** (N/m^2)	$\mathbf{Re_p}$	$\mathbf{w_\alpha}$
Open	2.03	0.16	0.40	363.85	0.48
Mild	1.83	0.26	0.77	533.00	0.63
Severe	1.24	0.48	3.57	666.76	0.42
Mild ETV	1.83	0.16	0.43	328.00	0.63
Severe ETV	1.24	0.07	0.36	97.23	0.42

Table 2 – The values of hydraulic diameter (D_h), peak velocity, wall shear stress, peak Reynolds number and Womersley number for an open, mild and severely stenosed Aqueduct of Sylvius. Values for endoscopic third ventriculostomy (ETV) are also displayed when applied to the mild and severe cases.

Site	$\mathbf{D_h}$	$\mathbf{v_p}$ (m/s)	**WSS** (N/m^2)	$\mathbf{w_\alpha}$
AS	2.03	0.16/0.09/ 0.16/0.10	0.24/0.24 / 0.4/0.24	0.48
LFL	6.08	0.03/0.02/0.02/0.02	0.08/0.06/0.05/0.04	2.08
RFL	4.79	**O** / 0.02 / **O** / 0.02	**O** / 0.05 / **O** / 0.04	1.64
FOM	5.10	0.03 / **O** / 0.02 / **O**	0.09 / **O** / 0.04 / **O**	1.74
CC	2.53	0.02/0.02/0.01/ 0.01	0.11/0.04/ 0.11/0.03	0.87

Table 3 – This table shows the values of hydraulic diameter ($\times 10^{-3}\ m$), peak velocity, wall shear stress and Womersley number for the AS, LFL, RFL, FOM and CC when the RFL and FOM have been fully occluded. In addition, the two conditions are repeated to display values when ETV has been applied. There a four separate values for v_p and WSS. From right to left these are: RFL occlusion/ FOM occlusion/ RFL occlusion + ETV/ FOM occlusion + ETV. *O* indicates full occlusion.

where, $(\partial u/\partial y)$ denotes the strain rate at the ventricular wall.

From Table 2 it can be seen that increasing the severity of aqueductal stenosis increases the WSS from a value of $0.4\ N/m^2$ in the open aqueduct, to $3.57\ N/m^2$ in the severely stenosed case. In turn, introducing ETV can reduce the WSS by nearly one order of magnitude back to $0.36\ N/m^2$. Observing the results in Table 3, one can confirm that the aqueduct possessed a reduced WSS when ETV is applied to the occlusion of the RFL (0.24 N/m^2), but, no evident reduction when considering the complete occlusion of the FOM. Both foramina of Luschka displayed reductions in WSS after introducing ETV. The CC showed a slightly stronger reduction in WSS when the FOM was fully occluded, and under the influence of ETV intervention (from 0.04 to $0.03\ N/m^2$). No change in the WSS of the CC was witnessed when the RFL was occluded (0.11 N/m^2).

4. Discussion

It was evident form the results in this study that the CC possessed the lowest peak velocity and simultaneously the lowest WSS ($0.03\ N/m^2$). This implies, from an anatomical point of view, that the CC acts more of a cushioning system for the spinal cord. This is in agreement with other results in the field (Loth, 2001; Gupta S. S., 2009; Gupta S. S., 2010). The Womersley number of the CC is close to the unity threshold (0.87), which as seen from Figure 5 (left), implied the inertial forces are beginning to be more taxing on the parabolic velocity profile. In Figure 5 (left), all degrees of occlusion (at $t = 0s$ and $t = 15s$) stated earlier are taken into consideration. As was the case for the 2nd and 3rd quadrants of Figure 4, the mildly stenosed aqueduct showed counter-intuitive characteristics. It may be that the mild case of aqueductal stenosis which had a 50% higher Womersley number than the severe case of stenosed configurations plays an important role. On the right hand side of Figure 5, the velocity profile of the LFL outlet is shown at the last simulation step ($t = 15s$). All cases of

Occlusion	Re_{AS}	Re_{RFL}	Re_{LFL}	Re_{FOM}	Re_{cc}
RFL	363.85		197.52	165.68	56.68
FOM	204.67	107.32	136.22		56.68
RFL ETV	363.85		136.22	114.26	28.34
FOM ETV	227.41	107.32	136.22		28.34

Table 4 – This table shows the values of Reynolds number for RFL, LFL, CC, AS and FOM when the LFL and FOM have been *completely* occluded. The corresponding values when ETV is applied are also shown.

occlusion are considered once more. It can be seen that increasing the aqueductal stenosis actually decreases the peak velocity of the profile. Blocking the sister RFL increases the overall peak velocity passing through the LFL more profoundly than the occlusion of the FOM. Finally, applying ETV eases the velocity magnitude in both the latter cases. These conceptual results allow one to appreciate the importance of the AS and the overall sensitivity of the VS geometry. This is emphasised by the importance of the hydraulic diameter of the aqueduct, and although it can be seen from Table 2 that $D_{h_{severe}} < D_{h_{mild}}$, the relationship of this parameter to the underlying axial component lengths (ratio a/b, contributing to the elliptical perimeter) become important.

It must be noted that maximum geometrical detail was attempted for the VS, CP and incoming arteries, however owing to the limited resolution of the MRI data the precise μm scale vascular structures within the CP and its precise sponge-like complexity was impossible to capture. In addition, there was conflation of the anterior and posterior choroidal arteries that influence the LV. This was done for simplicity, and was compensated by increasing the diameter of the inlets in those boundaries. The porosity of the CP was kept isotropic at a constant value of 0.5 (permeability $10^{-10}\, m^2$) since the boundary condition for the arterial inlets at the CP of the LV was elevated to 2000 Pa to account for the distinction of conflating the arteries leading to the aforementioned CP.

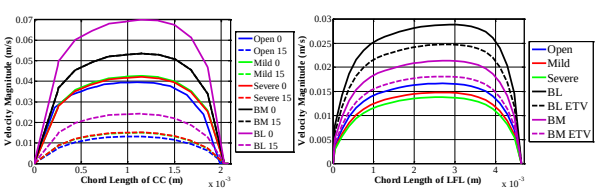

Figure 5 – Profiles of Velocity Magnitude (m/s) for CC and LFL under varying degrees of stenosis and/or occlusion.

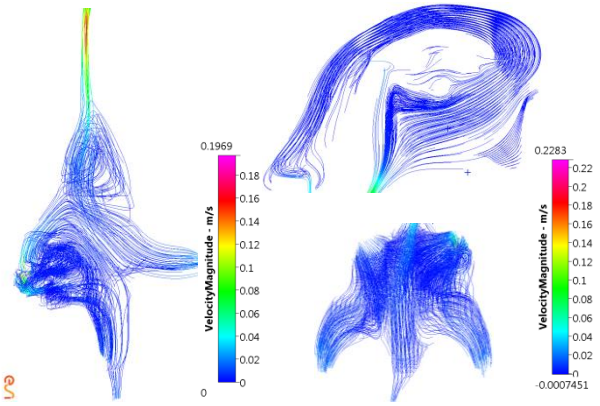

Figure 6 – Lines tangent to the instantaneous velocity vector of AS and 4th ventricle (left), 3rd ventricle and LV (top right) of occluded RFL case. The 4th ventricle of the mildly stenosed AS case is also shown as a comparison (bottom right) to the 4th ventricle on the left.

It is evident that the anatomy of the fourth ventricle is more complicated than the LV, 3rd Ventricle and AS. Substantially complicated flow patterns were observed in all three spatial directions (Figure 6). In addition, this flow is dependent on the splitting of the caudal flow from the mediating AS. This is in agreement with recent work in CSF patterns in the cerebral ventricles (Stadlbauer, 2010). Quantifiable evidence of CSF flow asymmetry in the ventricular system is shown from the peak velocity, WSS and velocity streamlines obtained (Figure 6). The application of ETV on the applied cases of acute stenosis of the aqueduct amplified the need to stress the importance of the AS as a mediator of the development of acute and possibly normal pressure hydrocephalus; especially when considering ventriculomegaly as a tangible marker of the extent of the disease. In addition, the amplified ventriculomegaly during applied ETV intervention for the cases of unforeseen foramina atresia in the fourth ventricle may be better served by considering endoscopic fourth ventriculostomy (Gianetti, 2011) to avoid the efforts of the mediating AS to distort CSF flow.

The assumptions made in constructing the MPET model allow for useful inferences to be made. The realm of ventriculomegaly and applied ETV when considering a very anatomically accurate VS representation along with its CSF actuators, namely the CP and their constituent arteries cater for this statement. The ideal scenario would involve

relaxing the quasi-steady assumption in order to provide insight into the effects of different forms of pulsatility applied to the system. The addition of an anatomically accurate venous system within the CP and the orientation of the Interthalamic adhesion may yield further important depictions of ventriculomegaly and exotic CSF flow characteristics. Cellular lever interactions such as those associated with the presence of aquaporins (Agre, 2006) should also be considered in an MPET framework, as their inclusion may prove pivotal in defining the critical complexity associated with CSF transport within the VS.

5. Conclusions

This work discusses a novel application of endoscopic third ventriculostomy to an anatomically accurate ventricular system utilising the MPET mathematical framework. The sites of CSF production, namely the choroid plexus of the lateral, third and fourth ventricles along with their incoming arterial networks are introduced for the first time in such a model.

The advantage of using the MPET representation here is that it allows the investigation of fluid transport between CSF, brain parenchyma and cerebral blood. In this study, ventriculomegaly was evident in three cases of aqueductal stenosis, along with the separate study of the atresia of the foramina of Magendie and right Luschka. Increasing the input pressure boundary condition increases the CSF velocity through the ventricular system but no noticeable net pressure changes are apparent.

The advantage of interrogating the effect of endoscopic techniques such as ETV allowed conduits to be made between the sensitive anatomical characteristics of the aqueduct of Sylvius, the fourth ventricle and the effective outlet velocity profiles. The use of the Womersley number and wall shear stress aided this analysis. Added emphasis can be given to the effects of splitting the jet flow of CSF leading from the aqueduct of Sylvius to the fourth ventricle, where the asymmetric flow interactions and resulting flow dynamics may prove pivotal in outlining a successful future treatment method in that of fourth ventriculostomy to the disease of hydrocephalus.

6. Acknowledgements

The support of the Digital Economy Programme is kindly acknowledged. This is a Research Councils UK cross council initiative led by EPSRC and contributed to by AHRC, ESRC, and MRC. Dr M. Megahed and the ESI Group are kindly acknowledged for allowing the use of the CFD-ACE+ suite.

The EPSRC is further acknowledged for providing the resources necessary for the High Performance Computing simulations conducted in this study.

7. References

Agre, P. (2006). The Aquaporin Water Channels. *Proceedings of the American Thoracic Society, 3*, 5-13.

Bai, M. E.-C. (1993). Multiporosity/Multipermeability Approach to the Simulation of NAturally Fractured Reservoirs. *Water Resources Research, 29*(6), 1621-1633.

Bulat, M. K. (2011). Recent insights into a new hydrodynamics of cerebrospinal fluid. *Brain Research Reviews, 65*, 99-112.

Cheng, S. B. (2010). The effects of interthalamic adhesion position on cerebrospinal fluid dynamics in the cerebral ventricles. *Biomechanics, 43*, 579-582.

Farin, A. A. (2006). Endoscopic third ventriculostomy. *Clinical Neuroscience, 13*, 763-770.

Gianetti, A. M. (2011). Fourth ventriculostomy: an alternative treatment for hydrocephalus due to atresia of the Magendie and Luschka foramina. *Neurosurgical Pediatrics, 7*, 152-156.

Gupta, S. S. (2009). Three-Dimensional Computational Modeling of Subject-Specific Cerebrospinal Fluid Flow in the Subarachnoid Space. *Biomechanical Engineering, 131*.

Gupta, S. S. (2010). Cerebrospinal fluid dynamics in the human cranial subarachnoid space: an overlooked mediator of cerebral disease. I. Computational model. *Royal Society of Interface*, 1-10.

Hellwig, D. G. (2005). Endoscopic third ventriculostomy for obstructive hydrocephalus. *Neurosurgical Review, 28*, 1-34.

Howden, L. G. (2007). Three-dimensional cerebrospinal fluid flow within the human vetricular system. *Computer Methods in Biomechanics and Biomedical Engineering, 11*(2), 123-133.

Irani, D. (2009). *Cerebrospinal Fluid in Clinical Practice.* Philadelphia, PA, USA: Saunders Elsevier.

Loth, F. Y. (2001). Hydrodynamic Modeling of Cerebrospinal Fluid Motion Within the Spinal Cavity. *Biomechanical Engineering, 123*, 71-79.

Marinkovic, S. G. (2005). Microanatomy of the Intrachoroidal Vasculature of the Lateral Ventricle. *Operative Neurosurgery, 57*(1), 22-36.

Rekate, H. (2008). The definition and classification of hydrocephalus: a personal recommendation to stimulate debate. *Cerebrospinal Fluid Research, 5*(2), 1-7.

Shojima, M. M. (2001). Magnitude and Role of Wall Shear Stress on Cerebral Aneurysm. *Stroke, 35*, 2500-2505.

Stadlbauer, A. S. (2010). Insight into the patterns of cerebrospinal fluid flow in the human ventricular system using MR velocity mapping. *NeuroImage, 51*, 42-52.

Sweetman, B. X. (2011). Three-dimensional computational prediction of cerebrospinal fluid flow in the human brain. *Computers in Biology and Medicine, 41*, 67-75.

Thompson, D. (2009). Hydrocephalus. *Neurosurgery, 27*(3), 130-134.

Tully, B. B. (2010). Is Normal Pressure Hydrocephalus More Than a Mechanical Disruption to CSF Flow. *32nd Annual International Conference of the IEEE EMBS*, (pp. 235-238). Buenos Aires.

Tully, B. V. (2010). Cerebral water transport using multiple-network poroelastic theory: application to normal pressure hydrocephalus. *Fluid Mechanics, 667*, 188-215.